J MATER SCI 41 (2006) 1445–1448

Supercritical hydrothermal synthesis of organic-inorganic hybrid nanoparticles

T. MOUSAVAND, S. TAKAMI, M. UMETSU, S. OHARA, T. ADSCHIRI*
2-1-1 Katahira, Aoba-ku, Sendai, 980-8577, JAPAN
E-mail: ajiri@tagen.tohoku.ac.jp

Abstract We have developed supercritical hydrothermal synthesis method of metal oxide nanoparticles where metal salt aqueous solution is mixed with high temperature water to rapidly increase the temperature of the metal salt solution and thus reduce the reactions and crystallizations during the heating up period. By using this method, we succeeded in the continuous and rapid production of metal oxide nanocrystals.
A new method proposes to synthesize organic-inorganic fused materials based on the methods of supercritical hydrothermal synthesis. By introducing organic materials in a reaction atmosphere of supercritical hydrothermal synthesis, we successfully synthesized metal oxide nanoparticles whose surface was modified with organic materials. In supercritical state, water and organic materials form a homogeneous phase, which provides an excellent reaction atmosphere for the organic modification of nanoparticles. Modification with bio-materials including amino acids was also possible. By changing organic modifiers, particle morphology and crystal structure were changed.
This organic surface modification provides a various unique characteristics for the nanoparticles: Dispersion of nanoparticles in aqueous solutions, organic solvents or in liquid polymers can be controlled by selecting hydrophilic or hydrophobic modifiers.

1. Introduction

Nanotechnology is defined as a technology to use materials whose dimension is in the range from 0.1 to 100 nm and thus physical and chemical properties are different from bulk one. Nanoparticles are considered as essential materials in nanotechnology. Physical and chemical properties of nanoparticles can be varied by changing size and morphology of the nanoparticles. Especially the size of the particles reflects in the increase in the ratio of surface to volume as surface or interface induced effect. The size effect, in particular the quantum size, is mainly considered to describe physical properties (the quantum size effect appears where the normal bulk electronic structure is replaced by a series of discrete electronic levels). While the surface or interface induced effect plays an important role for chemical processing [1]. For example, the increase in the performance of catalysis and structures such as electrodes for the improvement of such technologies as fuel cells and batteries is because of the surface or interface induced effect. However in the size effect, when the size of nanoparticles is lower than critical wavelength of light (less than 100 nm), a useful property as transparent which can be applied in packaging, cosmetics and coating will be appeared [2]. In biotechnology, labeling of cell by fluorescent nanoparticles and hyperthermia with magnetic nanoparticles are interested for applications of nanoparticles in biomedical aspects [1].

Production of nanoparticles can be carried out by chemical and physical methods. We proposed an original method of supercritical hydrothermal synthesis to produce nanoparticles [3–5]. Conventional hydrothermal synthesis of metal oxides from aqueous solutions is typically utilized at temperature ranging from 373 K to 473 K and in a batch-type autoclave reactor. In the proposed method with a flow type tubular reactor, metal salt aqueous solution was mixed with high temperature water to increase the solution temperature rapidly up to the supercritical state. Because of the high reaction rate of hydrothermal

*Author to whom all correspondence should be addressed.
0022-2461
DOI: 10.1007/s10853-006-7458-y

synthesis and low solubility of metal oxides, extremely high super saturation degree is attained just after the mixing point. This leads to the formation of nano meter size particles [3–5].

Successful application of nanoparticles includes using inorganic nanoparticles as filler in polymers to improve barrier properties, electrical conductivity and refractive index depends on their proper disperse into the fluids [6]. However, metal oxide nanoparticles produced in a water phase, due to the presence of hydroxyl groups on their surface, can not easily be dispersed in a non-polar organic material, unless a dispersing agent is used. A proper surface modifier can prevent particle growth and the surface modification of nanoparticles improves dispersion property as well as chemical, electrochemical resistance and optical appearance properties [6]. If metal oxides can be modified very well, a large number of new or improved engineering products can be produced. Furthermore, once the nanoparticles are modified with amino acids, peptides, proteins, or DNA, the particles can be specifically combined with other proteins or DNA, which leads to the applications to new biotechnology or IT devices using programmed assembly of semiconductor nanoparticles.

There are some methods for surface modification of metal oxide particles, including silane coupling for surface modification of oxides. In silane coupling, the metal oxides must be dipped into an organic solution. Since the surface of metal oxide nanoparticles is surrounded by hydroxyl groups (hydrophilic), they can't easily be dispersed in that solution for surface modification. Another method as CNBr activation can't be used for surface modification because the reaction media is acidic and can dissolve metal oxide nanoparticles [7]. Thus, these methods can't be used as suitable manner for surface modification of metal oxide nanoparticles.

In this paper, we will describe in situ surface modification of nanoparticles in sub-critical and supercritical conditions at 200, 300 and 400°C by hydrothermal synthesis as an attractive method for production of metal oxide nanoparticles. Because of the formation of homogeneous reaction atmosphere for organic modifiers and high temeprature water, organic-inorganic reactions successfully proceed to form organic-inorganic hybrid nano particles. We used various kinds of organic modifier and metal oxides systems.

2. Experimental

2.1. Reagents

$Al(NO_3)_3$, $Ce(NO_3)_3$, $CoSO_4$, $Fe(NO_3)_3$, $FeSO_4$, $Ni(NO_3)_2$, $Ti(SO_4)_2$, $Zn(NO_3)$, and $Zr(NO_3)_4$ were used as starting materials in this study and were purchased from Wako Chemicals Ltd. CeO_2, CO_2O_3, Fe_2O_3, NiO, SiO_2, SnO_2, TiO_2, and ZnO particles purchased from Wako Chemicals were also used. Surface modifiers used were alcohols, aldhydes, carboxylic acids, amines, thriols with C6, C8 and C10 hydrocarbons and alginic acid, which were from Wako Chemicals Ltd. Water was distilled by EYELA STILL ACE SA-2100E and used for hydrothermal synthesis.

2.2. Hydrothermal synthesis and surface modification in subcritical and supercritical water

Pressure-resistant tube reactors (SUS 316) whose inner volume was 5.0 mL were used for hydrothermal synthesis with in-situ surface modification. The reactor was loaded with 2.5 mL of 0.1 M of metal salt aqueous solution. In order to modify the surface of metal oxide nanoparticles, 0.1 mL of the surface modifier was added. The reactors were then capped tightly and put in an electric furnace whose temperature was maintained at 200, 300 or 400°C. The reaction was performed for 10 min and terminated by quenching the reactor in a water bath. After quenched, the reactor was washed by distilled water and isooctane in turn to collect solid products. The obtained products were purified by three cycles of a combination of decantation and centrifugation using ethanol. Then similar procedure was performed twice using distilled water. Finally, the products were purified with ethanol and dried.

2.3. Characterization

The crystallographic identity of the solid products was evaluated by X-ray diffraction (XRD) measurement. The size and shape of the nanoparticles were studied by using the transmission electron microscopy (TEM, JEM-1200 EXII (JEOL, Ltd.)). The chemical bonds on the surface of products were evaluated by Fourier transform infrared spectroscopy (FTIR).

3. Results and discussion

First, a seris of experiments was conducted to examine reactions of modifiers and metal oxide surface. Particles were loaded in a 5 ml of autoclave with a surface mofidier (0.1 ml) and water (2.5 ml.). The reactor was heated up to 473, 573 or 673 K and kept at the temperature for 10 min. The products were recovered in two phase solvents of water and chloroform. Fig. 1 shows the results of hexanal treatment for TiO_2 at 673 K. As shown in this photo, original particles were dispersed in a water phase, but organic treated particles were dispersed in a chloroform phase. This suggests that the surface of TiO^2 were modified with organic molecules during the treatment in high temperature water. By the FTIR analysis, we confirmed the hyxanal were chemically bonded on the surface of TiO_2, which will be discussed later.

Fig. 2 shows a TEM image of Fe_2O_3 nanoparticles obtained by in-situ reaction and modification experiment, namely hydrothermal synthesis with dodeconoic acid. As

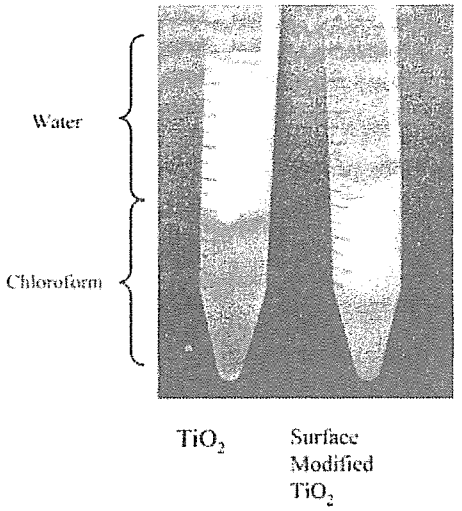

Figure 1 Control of dispersion of nano particles in water and organic solvent.

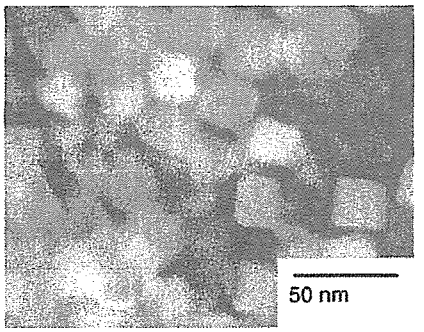

Figure 2 TEM image of decanoic acid modifed Fe_2O_3 nano particles

show here, around 10–20 nano meter size of particles could be obtained. Particle size distribution was very narrow and the facet could be observed even for these nano size particles, which implies formation of single crystal.

Fig. 3 shows XRD patterns of surface modified nanoparticles of cobalt oxide. Even for the nano meter size particles, relatively sharp peaks were obtained. This also suggests the high crystallinity of the obtained products.

For the experiments for CO_3O_4, particles, size were compared for with and without a modifier, hexylamine. The average size of the nanoparticles was (a) 50 nm for products without modifier and (b) 20 nm for products with the modifier. It was observed in the case of CO_3O_4 that (a) the nanoparticles synthesized without modifier have their own particular crystalline structure while (b) nanoparticles with modifier have spherical shape, for the case of CO_3O_4. These results indicate that the modifier attached on growing surfaces of the nanoparticles and changed to their energetic stability that closely relates to the size and crystalline structure of nanocrystals. TEM results also implies that using the modifiers can prevent from agglomeration between cobalt oxides nanoparticles and the size of particles decreases as well as temperature increases.

FTIR analysis was used for investigation of formed bands between nanoparticles and modifiers due to the chemical interaction. Fig. 4 shows an FTIR spectra for dodecanylacid treatment on Fe_2O_3. As shown in this figure, peaks of CH_2 and CO functional groups could be observed. This clearly indicates the formation of chemical bonding between the surface of metal oxide and docecanylacid. Also for the other modifiers and metal oxides, chemical bond formation was observed, although the conditions were different among the systems.

The process of reaction by these modifiers may be described as the following reactions:

$$\text{MO-(OH)}_X + \text{y(HO-R)} = \text{MO-(OH)}_{x-y}\ \text{y(O-R)} + \text{y}H_2O \quad (1)$$

$$\text{MO-(OH)}_x + \text{y}(H_2\text{N-R}) = \text{MO-(OH)}_{x-y}\ \text{y(H-N-R)} + \text{y}H_2O \quad (2)$$

$$\text{MO-(OH)}_x + \text{y(HC(O)-R)} = \text{MO-(OH)}_{x-y}\ \text{y(C(O)-R)} + \text{y}H_2O \quad (3)$$

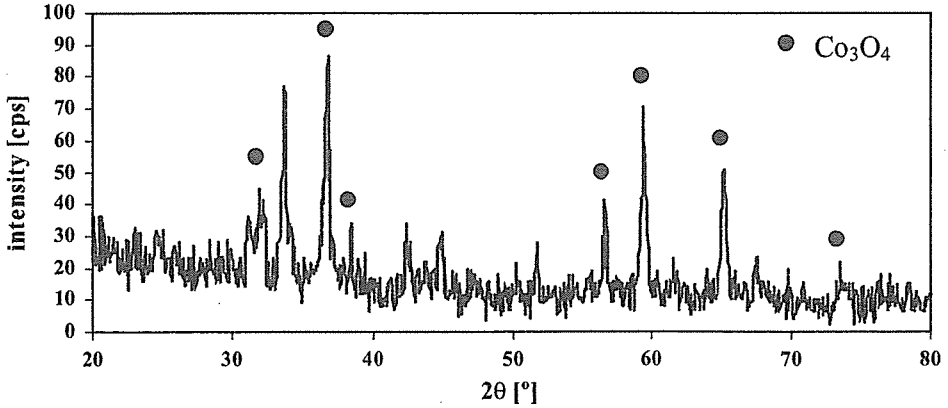

Figure 3 XRD patttern for hexanal modifed Co_3O_4.

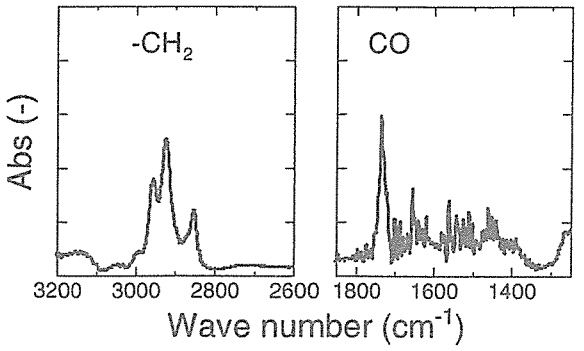

Figure 4 FTIR spectra of $C_9H_{19}COOH$ modified nanoparticles.

$$MO\text{-}(OH)_x + y(HOC(O)\text{-}R) = MO\text{-}(OH)_{x-y}\ y(OC(O) - R) + yH_2O \quad (4)$$

The optimum conditions for the surface modification differ among the modifiers and metal oxides. For the case of modification of cobalt oxides with hexyl functional groups, only C_5-CHO at 400°C and C_6-NH_2 at every temperature (200, 300 and 400°C) can modify the surface. But C_6-SH can't work for surface modification at 400°C. In spite of presence of some particles in organic phase, XRD showed that these products are some kind of cobalt sulfide compositions and there is not any cobalt oxide.

It was also confirmed that amino acids (alginic acid) modification of metal oxide nanoparticles was possible for iron oxide. According to the results of the experiments of amine and carboxylic acid, amino functional group of alginic acid may react with hydroxyl groups of metal oxide surface. The amino acids modified nano particles look like polymer, rather than solid powders. This is probably due to self-assembly of nanoparticles through the specific interaction of amino group and carboxylic group on the surface of nanoparticles. This kind of bio-modification of nano particles paves a way to the programmed assembly of nanoparticles for the fubrications of IT devices.

Acknowledgment

This research was partially supported by the Ministry of Education, Culture, Sports, Science and Technology, a Grant-in-Aid for the COE project, Giant Molecules and Complex Systems, 2002.

References

1. J. DUTTA and H. HOFMANN, *Nanomaterials, Swiss Federal Institute of Technology, December* (2003) pp. 9–20
2. P. HOLISTER, J. W. WEENER, C. ROMAN and T. HARPER, *Nanoparticles, Technology White Papers', (Cientifica,* October 2003) 5–7
3. T. ADSCHIRI, K. KANAZAWA and K. ARAI, *J. Am. Ceram. Soc.* **75** (1992) 1019–1023.
4. T. ADSCHIRI, Y. HAKUTA, K. SUE and K. ARAI, *The Journal of Nanoparticle Research*, **3** No. (2–3) (2001) 227.
5. T. ADSCHIRI and K. ARAI, *Supercritical Fluid Technology in Materials Science and Engineering, Ed. Ya-Ping Sun, Marcel Dekker INC.* (2003) *Tokyo.*
6. W. POSTHUMUS, P. C. M. M. MAGUSIN and *et. al., J. Colloid and Interface Science* **269** (2004) 109
7. S. P. COLOWICK and N. O. KAPLAN, *Methods in enzymology Part C; Jakoby*, W. B.; ACADEMIC Press INC: New York (1987) 3–6.

Received 19 October 2004
and accepted 28 April 2005

Japanese Journal of Applied Physics
Vol. 45, No. 3A, 2006, pp. 1836–1840

Optical Visualization of Ultrasound Pressure Fields in Turbid Media Based on Coherent Detection Imaging Technique

Masaki KOBAYASHI*, Takafumi KASAMATSU, Yukihiro SHIBUYA and Masaru ENOMOTO

Department of Electronics, Tohoku Institute of Technology, 35-1 Yagiyama Kasumicho, Taihaku-ku, Sendai 982-8577, Japan

(Received August 19, 2005; accepted December 2, 2005; published online March 8, 2006)

An optical method for visualizing ultrasound fields in turbid media is described. A laser beam is modulated by ultrasound waves in a light-scattering medium and is detected using a coherent detection imaging technique based on the optical heterodyne method. We demonstrate for the first time the ability to visualize the profile of an ultrasound field generated by a focus-type ultrasound transducer. This is achieved by utilizing forward-scattered light originating from a laser beam that is phase modulated by Raman–Nath diffraction and is also modulated in amplitude through the density variation of scatters in a test medium and/or a small amount of beam deflection. In this study, we demonstrate the two-dimensional determination of a sound field, even in an optically turbid medium. [DOI: 10.1143/JJAP.45.1836]

KEYWORDS: ultrasound, sound pressure, acoustooptic effect, imaging, visualization, light scattering, coherent detection imaging, CDI, optical detection

1. Introduction

Many optical methods for visualizing ultrasound fields propagating in liquid or air have been developed and employed for practical measurements.[1,2] These methods, of which the Schlieren method is a typical example, are mostly based on imaging a phase object originating from a dispersion of the refractive index. Although these techniques have the advantage of a high sensitivity for measuring sound pressure without any perturbation of the field, they can usually only be applied to transparent media. Recent advances in the development of optical measurement techniques for characterizing the spatial distribution of optical absorption within light-scattering media such as living tissue have been remarkable. The coherent detection imaging (CDI) technique is a method for visualizing the internal structure of light-scattering media through the extraction of the boundaries of the refractive indices and/or for imaging the distribution of absorbing pigments embedded in light-scattering media.[3–6] This technique is characterized by excellent directionality, and selectivity and high sensitivity, leading to a wide dynamic range for detecting straightforward on-axis scattered light on the basis of the optical heterodyne technique, often referred to as "coherent gating". We have applied this technique to determine sound-pressure fields propagating in opaque media. In this paper, we propose a novel method for visualizing the sound-pressure field in a water-based light-scattering medium and demonstrate two-dimensional images that are measured in focused sound fields.

2. Methods and Materials

2.1 Setup

The experimental setup, as shown in Fig. 1, is based on a Mach–Zehnder interferometer, composed of a continuous wave Ti:Al_2O_3 laser system as a coherent light source, a pair of acoustooptic modulators (AOMs) as frequency shifters and a Si p–i–n photodiode as a detector. The laser beam is reduced and collimated to a diameter of 1 mm and split into a signal beam and a local oscillator beam via a polarized beam splitter. The frequencies of these beams are shifted by the AOMs to 80 and 80.1 MHz, respectively. The signal beam passes through a water tank, which has a physical path length of 100 mm, and is then mixed with the local oscillator beam via a beam-splitter and impinges on a Si p–i–n photodiode. The signal is fed into a spectrum analyzer and the intensities of the intermediate frequencies (IFs) are recorded using a personal computer. The dynamic range of the intensity in our frequency range was 110 dB. A focus-type ultrasonic transducer (GE Panametrix, V315-SU; focal length: 55 mm, focal diameter: 0.3 mm) driven by a 10 MHz continuous sinusoidal wave (70 V_{p-p}) is incorporated into the side wall of the water tank in which the ultrasound beam traverses the laser beam.

In this configuration, which is characterized by a small acoustooptic interaction length and a relatively low frequency of the ultrasound, the acoustooptic effect can be described as being caused by the Raman–Nath theory. The Klein–Cook parameter Q is estimated to be 6.5×10^{-2} in the focal zone of the ultrasound beam. In transparent media, an incident beam interacts with a sound field and is diffracted through a phase grating. This phenomenon engenders both ±1st order splitting (which involves a Doppler shift of the light frequency by ±10 MHz) and a 0th order component without any frequency shift. The Raman–Nath theory describes the phase modulation of the diffracted beam at ultrasonic frequencies to provide information regarding sound pressure.[7,8] However, in a scattering medium, the nature of light scattering in an ultrasound field appends other factors to the amplitude modulation; these factors originate from the density variation of scatters caused by their displacement and induce periodic changes in scattering coefficient.[9–13] If even a fraction of the laser light remains coherent under multiple-scattering conditions, it can interfere with the local oscillation beam, implying the possibility of extracting the straightforward scattered-beam component and the accompanying characteristics of the sound field on-axis to the beam. The modulation of the signal beam in phase is characterized by the sound pressure expressed as a Raman–Nath parameter originating from the variation in refractive index that passes through the sound field. In addition, the modulation of the signal beam in amplitude is also characterized by sound pressure, which engenders the displacement of scatters and/or small deflection of the beam. Consequently, an output signal, comprising 100 kHz, 10 MHz, 10.1 MHz, and 9.9 MHz components and their

*E-mail address: masaki@tohtech.ac.jp

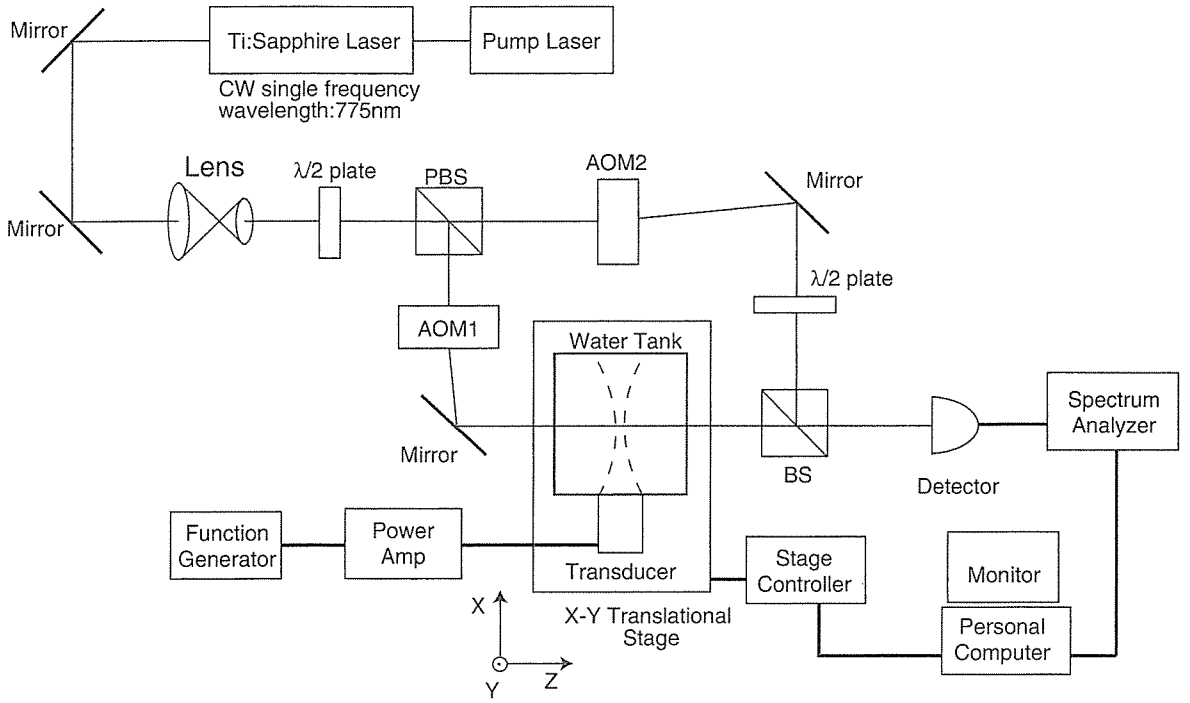

Fig. 1. Schematic of experimental setup. AOM1 and AOM2 are the acousto-optic modulators and PBS and BS are the polarized beam-splitter and the beam-splitter, respectively.

harmonics, is generated after mixing with the local oscillator beam, as described in the following section.

2.2 *Theoretical*

The analytical signals of the electric fields of the signal beam and the local oscillator beam can be expressed respectively as

$$V_S(t) = E_S \exp i(\omega_S t + \phi - \mathbf{k}_S \cdot \mathbf{r}) \quad (1)$$

$$V_L(t) = E_L \exp i(\omega_L t - \mathbf{k}_L \cdot \mathbf{r}), \quad (2)$$

where ω_S and ω_L are respectively the angular frequencies of the signal and local oscillator beams after the frequency shift through the AOMs, Ω is the driving frequency of the transducer expressed in angular frequency, E_S is the amplitude of the electric field modulated through the variation of scattering properties in an ultrasound field, and E_L is the amplitude of the local oscillator beam. In addition, $\mathbf{k}_S$ and $\mathbf{k}_L$ represent the wave-number vector of the signal beam and that of the local beam, respectively; $\mathbf{r}$ is the position vector. The phase difference between the signal and the local oscillator beam is denoted as ϕ. The irradiance of the mixed wave can be expressed as

$$\begin{aligned} I &= |V_S(t) + V_L(t)|^2 \\ &= |V_S|^2 + |V_L|^2 + (V_S \cdot V_L^* + V_S^* \cdot V_L). \end{aligned} \quad (3)$$

In eq. (1), when the signal beam is modulated in phase and with amplitude by the driving frequency of the transducer, ϕ and E_S are derived as

$$\phi = v \sin \Omega t \quad (4)$$

$$E_S = E_{SAC} \sin \Omega t + E_{SDC}, \quad (5)$$

where E_{SAC} and E_{SDC} respectively represent the modulated (AC) component and the unmodulated (DC) component of the signal amplitude, and v is the modulation index of the phase modulation characterized by the Raman–Nath parameter. Consequently, eq. (1) is expressed as the following.

$$\begin{aligned} V_S(t) &= (E_{SAC} \sin \Omega t + E_{SDC}) \exp i(\omega_S t + v \sin \Omega t - \mathbf{k}_S \cdot \mathbf{r}) \\ &= (E_{SAC} \sin \Omega t + E_{SDC}) \exp(i\omega_S t) \\ &\quad \cdot \exp(iv \sin \Omega t) \cdot \exp(-i\mathbf{k}_S \cdot \mathbf{r}) \\ &= (E_{SAC} \sin \Omega t + E_{SDC}) \exp(i\omega_S t) \\ &\quad \cdot \sum_{n=-\infty}^{\infty} J_n(v) \exp[i(n\Omega t - \mathbf{k}_{Sn} \cdot \mathbf{r})] \end{aligned} \quad (6)$$

In these equations, $J_n(v)$ is the n-th order of the Bessel function. In eq. (6), $\mathbf{k}_S$ is divided into components of diffraction denoted as $\mathbf{k}_{Sn}$, corresponding to the wavenumber vector of the n-th order of diffraction. With consideration up to the $\pm$1st order of the Bessel function, eq. (6) can be re-written as

$$\begin{aligned} V_S(t) = (E_{SAC} \sin \Omega t + E_{SDC}) \{ & J_0(v) \exp(-i\mathbf{k}_{S0} \cdot \mathbf{r}) \\ & + J_1(v) \exp[i(\Omega t - \mathbf{k}_{S1} \cdot \mathbf{r})] \\ & + J_{-1}(v) \exp[i(-\Omega t - \mathbf{k}_{S-1} \cdot \mathbf{r})] \} \cdot \exp(i\omega_S t). \end{aligned} \quad (7)$$

Hence, the third term in eq. (3), which represents the interference of both beams, is given as

$$\begin{aligned} &(V_S \cdot V_L^* + V_S^* \cdot V_L) \\ &= (E_{SAC} \sin \Omega t + E_{SDC}) E_L \left\{ \left[J_0(v) \int_S e^{-i\mathbf{k}_0 \cdot \mathbf{r}} \, dS \right. \right. \\ &\quad + J_1(v) e^{i\Omega t} \int_S e^{-i\mathbf{k}_1 \cdot \mathbf{r}} \, dS + J_{-1}(v) e^{-i\Omega t} \left. \int_S e^{-i\mathbf{k}_{-1} \cdot \mathbf{r}} \, dS \right] \cdot e^{i\omega t} \\ &\quad + \left[J_0(v) \int_S e^{i\mathbf{k}_0 \cdot \mathbf{r}} \, dS + J_1(v) e^{-i\Omega t} \int_S e^{i\mathbf{k}_1 \cdot \mathbf{r}} \, dS \right. \\ &\quad \left. \left. + J_{-1}(v) e^{i\Omega t} \int_S e^{i\mathbf{k}_{-1} \cdot \mathbf{r}} \, dS \right] \cdot e^{-i\omega t} \right\}, \end{aligned} \quad (8)$$

where $\omega = \omega_S - \omega_L$ represents the difference in angular frequency between the signal and the local beam, and $\mathbf{k}_n = \mathbf{k}_{Sn} - \mathbf{k}_L$ is the difference in the wave-number vector of the n-th order between the signal and local beams. The area of the mixed wave on a detector surface is denoted as S.

Here, the coordinate system is selected as the 0th order of the signal beam with the local beam propagates along the Z-axis after passing through the mixing optics, and ultrasound waves propagate in parallel with the X-axis, as shown in Fig. 1. Diffracted signal beams are on the X–Z plane. The photosensitive surface of a detector, equipped with a smaller photosensitive area than the laser beam diameter, is placed on the X–Y plane centered at $\mathbf{r}(0, 0, 0)$. In this arrangement, when the detector has a square active area with size D, the spatial component of the interference on the detector is given as

$$\int_S e^{\pm i\mathbf{k}_n\cdot\mathbf{r}}\,dS = D\int_{-D/2}^{D/2}\exp[\pm ik_n(\sin\theta_n)x]\,dx = D\frac{\sin\left(\frac{Dk_n}{2}\sin\theta_n\right)}{\frac{k_n}{2}\sin\theta_n}, \tag{9}$$

where $k_n = |\mathbf{k}_n|$ and θ_n is the diffraction angle of the n-th order of the signal beam, and x represents the position on the X-axis. Therefore, eq. (8) can be simplified as

$$\begin{aligned}
&(V_S\cdot V_L^* + V_S^*\cdot V_L)\\
&= (E_{SAC}\sin\Omega t + E_{SDC})E_L\cdot\{[J_0(v)A_0 + J_1(v)(\cos\Omega t)A_1\\
&\quad + J_{-1}(v)(\cos\Omega t)A_{-1}]\cdot(e^{i\omega t} + e^{-i\omega t})\\
&\quad + i[J_1(v)(\sin\Omega t)A_1 - J_{-1}(v)(\sin\Omega t)A_{-1}]\cdot(e^{i\omega t} - e^{-i\omega t})\}\\
&= J_0(v)\cdot A_0\cdot E_L\{2E_{SDC}\cos\omega t\\
&\quad + E_{SAC}[\sin(\Omega+\omega)t + \sin(\Omega-\omega)t]\}\\
&\quad + J_1(v)\cdot A_1\cdot E_L\{2E_{SDC}\cos(\Omega+\omega)t\\
&\quad + E_{SAC}[\sin(2\Omega+\omega)t - \sin\omega t]\}\\
&\quad + J_{-1}(v)\cdot A_{-1}\cdot E_L\{2E_{SDC}\cos(\Omega-\omega)t\\
&\quad + E_{SAC}[\sin(2\Omega-\omega)t + \sin\omega t]\},
\end{aligned} \tag{10}$$

where

$$A_n = D\frac{\sin\left(\frac{Dk_n}{2}\sin\theta_n\right)}{\frac{k_n}{2}\sin\theta_n}.$$

As shown in eq. (10), the interference signal contains the ω, $\Omega\pm\omega$, $2\Omega\pm\omega$ components of the frequency. The intensity ratio of these components depends on the angle formed by the signal beam and the local beam. To evaluate the selection of the different orders of the Raman–Nath diffraction component, we measured the changes in the intensity of two frequency components, $\Omega+\omega$ and $\Omega-\omega$, as a function of the mixing angle between the signal and the local beam. Figure 2(a) shows the result obtained in a transparent medium with the rotation of the mixing optics. The two curves show dominant peaks located at 0 and $\pm1.9\times10^{-3}$ rad with different ratios of the frequency components ($\Omega+\omega$ and $\Omega-\omega$), meaning that the $+1$st and -1st orders of the diffraction components are selected by mixing at the respective angles of -1.9×10^{-3} and $+1.9\times10^{-3}$ rad. In Fig. 2(a), however, the intensity of both components is shown to be maximized at 0 rad instead of $\pm1.9\times10^{-3}$ rad. This maximization is attributable to the lack of fine alignment in the mixing of the signal and local beams, which is accomplished merely by the rotation of the mixing optics and an axial transfer of the detector. Figure 2(b) shows data with the fine alignment of both beams at the five different rotational angles of 0, $\pm0.95\times10^{-3}$, and $\pm1.9\times10^{-3}$ rad, indicating that the angles that give the maximum intensity of the $\Omega+\omega$ and $\Omega-\omega$ components are located respectively at -1.9×10^{-3} and $+1.9\times10^{-3}$ rad. From this result, the selection of the ±1st order of diffraction angle and the detection of the corresponding $\Omega+\omega$ or $\Omega-\omega$ component which originates in phase modulation, is advantageous. Although $2\Omega\pm\omega$ components derived from amplitude modulation were also observed in the ±1st order of diffraction, these components were weak in comparison with $\Omega\pm\omega$ components. The

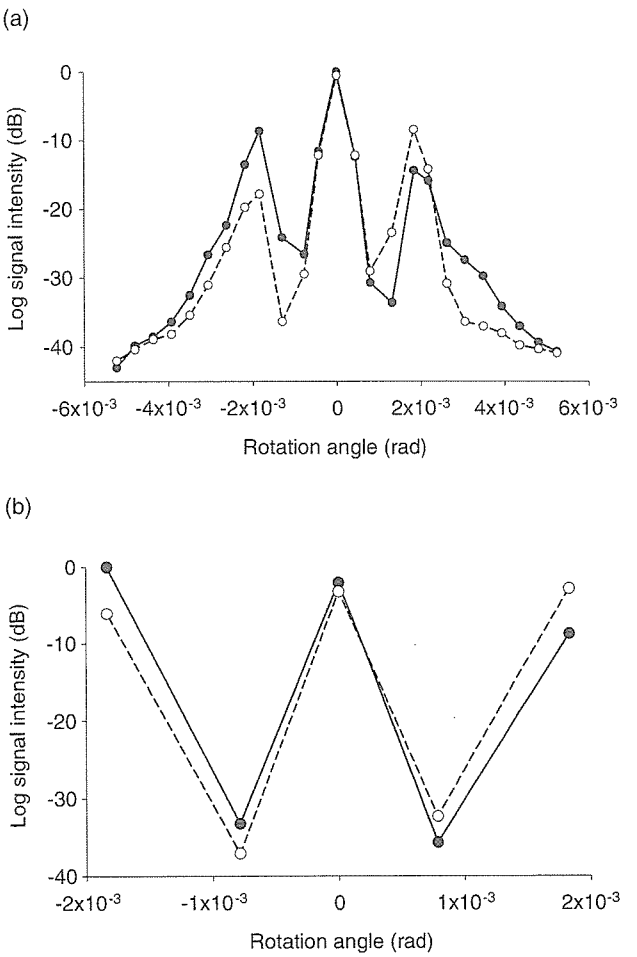

Fig. 2. Rotation angle of mixing beam splitter vs signal intensity of IF observed in the focal point of ultrasound field. The straight line with filled circles indicates the 9.9 MHz component of the IF signal and the dashed line with open circles indicates the 10.1 MHz component. (a) Obtained by rotation of beam splitter and X-axis transportation of detector. (b) Obtained after fine alignment of signal and local beams at angles of 0, $\pm0.95\times10^{-3}$, and $\pm1.9\times10^{-3}$ rad.

rotational angles of $\pm 1.9 \times 10^{-3}$ rad correspond to the reflection angles of $\pm 3.8 \times 10^{-3}$ rad on the mixing optics. In this configuration, from the Raman–Nath theory, the n-th order of diffraction angle is calculated as

$$\sin\theta_n = \frac{nK}{k_n} \cong \frac{n\lambda}{\Lambda\mu}, \tag{11}$$

where θ_n is the n-th order of diffraction angle and K is the wave-number of the ultrasound beam. In addition, Λ and λ respectively represent the wavelengths of the ultrasound and the light, and μ is the refractive index of the medium. In a water medium, using $\Lambda = 0.15$ mm and $\mu = 1.33$, θ_1 is derived as 3.88×10^{-3} rad corresponding to the observed angle that maximizes the 9.9 and 10.1 MHz frequency components in the IF signal.

In our experimental arrangement, the signal beam is aligned such that it selects the +1st order of the diffraction component for matching with the local beam. In this condition, the primary component of the IF signal is formed by the 9.9 MHz frequency component, with the other components by the 10 MHz, 10.1 MHz and their various harmonics. In contrast, when the −1st order of the diffraction component is selected, the signal is formed primarily by the 10.1 MHz frequency component.

2.3 *Experimental*

Throughout these experiments we used various concentrations of isotropic light-scattering media that were prepared by the dilution of Intralipid (Intralipid-10%; Fresenius Kabi AB, Sweden), which is a clinically used fat emulsion and often used for a tissue phantom to study the propagation of light in scattering media. The contents of 500 mL of Intralipid-10% are 50 g of soybean oil, 6 g of lecithin, 11.25 g of glycerin, and 430.5 g of water. It is reported that scattering particles consist of lecithin encapsulated soybean oil with an average diameter of 97 nm.[14] To observe the two-dimensional distribution of the sound field, the water tank was mounted on a two-axis translational stage and scanned in 500 μm steps along the X-axis and in 1 mm steps along the Y-axis (which are orthogonal to the incident laser beam) as shown in Fig. 1. All of the experiments were carried out using a wavelength of 775 nm and an incident beam signal intensity of 50 mW.

3. Results and Discussion

Experimentally obtained data regarding the concentration characteristics in terms of the signal intensity measured at the focal point of the ultrasound beam are shown in Fig. 3, including a comparison between two components with signals at 9.9 and 10 MHz, indicating a linear relationship between the concentration of the scattering centers and the log of the intensity of the output signals. The data of signal intensity in Fig. 3 is shown to be normalized by the intensity of the 9.9 MHz component at 0 mL/L. The minimum detectable level of the signal is therefore placed at −80 dB in this graph. The 9.9 MHz frequency component is able to produce a signal that is modulated by the sound field for a higher concentration of scattering centers than the 10 MHz frequency. When the concentration characteristics of the 9.9 MHz component represent the attenuation of the intensity of the laser beam as it passes on-axis through the

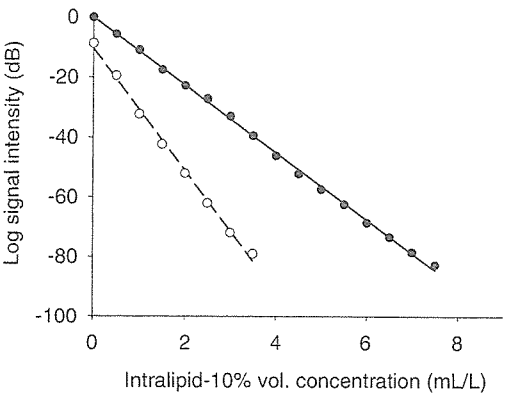

Fig. 3. Concentration of scattering media vs signal intensity of IF observed in focal point of ultrasound field. The straight line indicates the 9.9 MHz component of the IF signal and the dashed line indicates the 10 MHz component.

scattering medium, the slope of the line in Fig. 3 provides a scattering coefficient for the medium, which in this instance is 2.5×10^{-2} mL^{-1}·L·mm^{-1}. This nearly corresponds to the scattering coefficient of Intralipid-10% that has been reported elsewhere for 775 nm wavelength conditions.[15] On the other hand, although the 10 MHz frequency component also provides a signal under scattering conditions, the slope of the line for 10 MHz is steeper than that for 9.9 MHz, as shown in Fig. 3. This suggests that the generation of the 10 MHz frequency component (which is modulated in amplitude and contains a contribution from the multiple-scattered off-axis component) does not require matching with the local oscillator beam; therefore, this component of the signal is weakened (manifested as a reduction in intensity) through multiple scattering as the concentration of scattering centers increases. Figure 4 shows images that were obtained from the distribution of the focused sound field under different concentrations of scattering media (2, 4, 6, and 7 mL/L volume concentrations of Intralipid-10%). Although the intensity of the signal reduces to approximately −80 dB in the case of a 7 mL/L volume concentration of Intralipid-10%, the shape of the focused sound field shows the same pattern as the distributions observed for the other concentrations of scattering media. From the shapes observed under these different conditions, it is clear that the position of the focal point corresponds to the specification data of the transducer, indicating a focal length of 55 mm. Although a quantitative comparison is required for the application of this technique for the absolute measurements of the two-dimensional sound-pressure field, the results obtained here suggest that this method is potentially useful for qualitative measurements for determining the shape of the pressure field in a scattering medium. Taking this into consideration, further progress in the development of this technique for making quantitative measurements and expanding the dynamic range of heterodyne detection could provide a novel method for measuring ultrasound fields propagating in a variety of scattering media. Even in our experimental conditions, we used a water tank which has a 100 mm path length filled with the scattering medium for examinations; however, when this method is applied to an object which has a shorter path

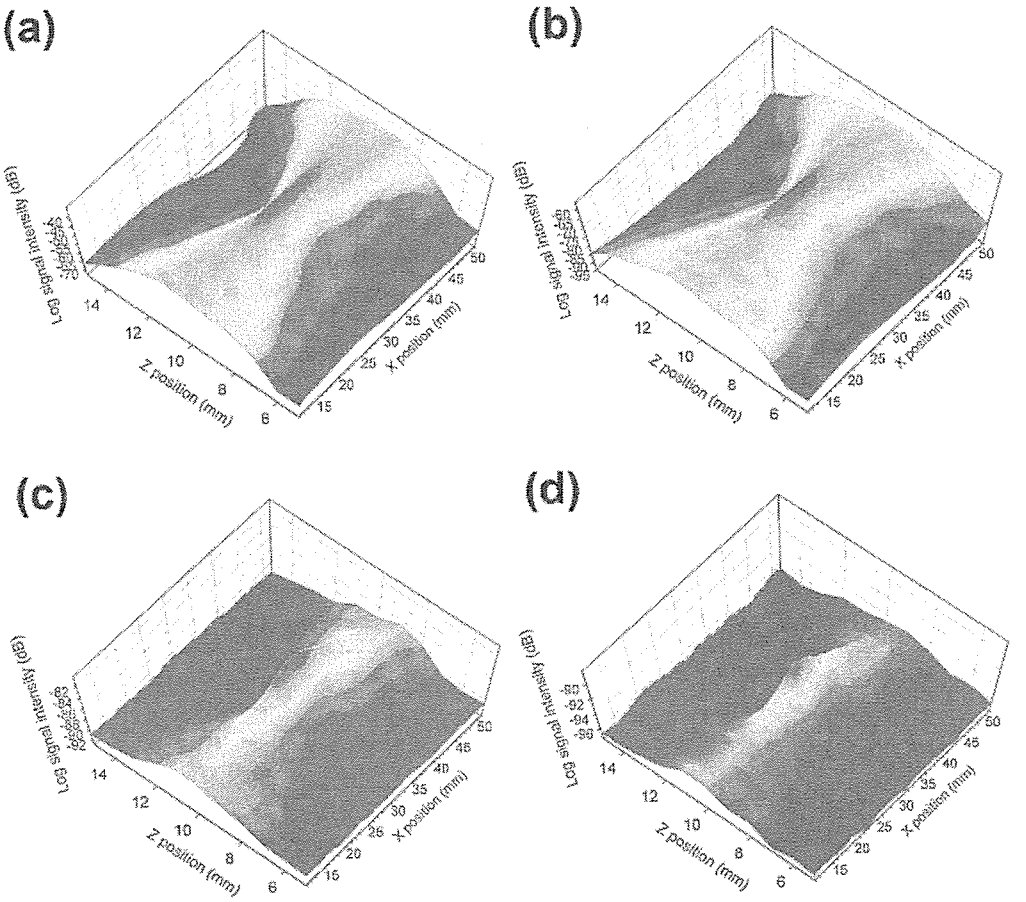

Fig. 4. Spatial distribution of ultrasonic fields for different concentrations of scattering media. (a) Volume concentration of Intralipid-10%, 2.0, (b) 4.0, (c) 6.0, and (d) 7.0 mL/L.

length, for example 20 mm, it is supposed to be detectable in an ultrasound field in the media with a scattering coefficient of approximately $1.0\,\mathrm{mm}^{-1}$.

In summary, we demonstrated a novel method for visualizing a sound field propagating in a light-scattering medium using a CDI technique, which utilizes the forward scattering of on-axis light that retains the coherence of the incident light. The on-axis characteristics of the sound field that affect the laser beam by modulating its phase and amplitude (originating from Raman–Nath diffraction for phase modulation, and the density variation of scatters and/or beam deflection for amplitude modulation) were determined. In this study, we have shown the capability of this technique for the two-dimensional determination of sound fields in turbid media through a demonstration using a water-based scattering solution of diluted Intralipid-10%, suggesting the potential of this technique for the visualization of the sound fields in opaque media. This technique is expected to contribute to the expansion of optical methods for the detection of sound fields.

Acknowledgment

This work was supported in part by grants from the Ministry of Education, Culture, Sports, Science and Technology of Japan and a special research grant from the Tohoku Institute of Technology.

1) T. H. Neighbors, W. G. Mayer and H. J. Ruf: J. Acoust. Soc. Am. **98** (1995) 1751.
2) K. L. Zankel and E. A. Hiedemann: J. Acoust. Soc. Am. **31** (1959) 44.
3) M. Toida, M. Kondo, T. Ichimura and H. Inaba: Appl. Phys. B **52** (1991) 391.
4) B. Devaraj, M. Kobayashi, M. Usa, M. Takeda, H. Inaba, H. Ishihata and H. Horiuchi: Electron. Lett. **31** (1995) 874.
5) B. Devaraj, M. Takeda, M. Kobayashi, M. Usa, K. P. Chan, Y. Watanabe, T. Yuasa, T. Akatsuka, M. Yamada and H. Inaba: Appl. Phys. Lett. **69** (1996) 3671.
6) B. Devaraj, M. Usa, K. P. Chan, T. Akatsuka and H. Inaba: IEEE J. Sel. Top. Quantum Electron. **2** (1996) 1008.
7) B. Cook: J. Acoust. Soc. Am. **60** (1976) 95.
8) S. Nagai and K. Iizuka: Jpn. J. Appl. Phys. **21** (1982) L505.
9) M. Kempe, M. Larionov, D. Zaslavsky and Z. Genack: J. Opt. Soc. Am. A **14** (1997) 1151.
10) G. D. Mahan, W. E. Engler, J. J. Tiemann and E. Uzgiris: Proc. Natl. Acad. Sci. U.S.A. **95** (1998) 14015.
11) L. V. Wang: Opt. Lett. **26** (2001) 1191.
12) L. V. Wang: Phys. Rev. Lett. **87** (2001) 043903.
13) S. Sakadzic and L. V. Wang: Phys. Rev. E **66** (2002) 026603.
14) H. Staveren, C. Moes, J. Marle, S. Prahl and M. Gemert: Appl. Opt. **30** (1991) 4507.
15) K. Fukuchi, B. Devaraj, M. Usa, M. Kobayashi, K. P. Chan and H. Inaba: Kogaku **27** (1998) 40 [in Japanese].

Available online at www.sciencedirect.com
SCIENCE DIRECT®
Journal of Photochemistry and Photobiology B: Biology 83 (2006) 69–76
Journal of Photochemistry and Photobiology B:Biology
www.elsevier.com/locate/jphotobiol

Technical communication

Anatomic characterization of human ultra-weak photon emission with a moveable photomultiplier and CCD imaging

Roeland Van Wijk [a,b,*], Masaki Kobayashi [c], Eduard P.A. Van Wijk [a]

[a] *International Institute of Biophysics, Raketenstation, Kapellener Strasse, D-41472 Neuss, Germany*
[b] *Faculty of Biology, Utrecht University, Padualaan 8, 3584CH Utrecht, The Netherlands*
[c] *Department of Electronics, Tohoku Institute of Technology, 35-1 Yagiyama Kasumicho, Sendai 982-8577, Japan*

Received 17 June 2005; received in revised form 26 October 2005; accepted 5 December 2005
Available online 18 January 2006

Abstract

Ultra-weak photon emission of a living system has received scientific attention because of its potential for monitoring oxidative metabolism and oxidative damage to tissues. Heretofore, most studies have focused only on the emission from hands. The data regarding emission from other anatomic locations are limited. A previous multi-anatomic site recording of four subjects quantitatively demonstrated that the emission from several corresponding anatomic locations could differ by as much as a factor of 4. The data also suggested a "common" anatomic emission percentage distribution pattern. This information raised the question whether such a typical anatomic percentage emission exists. The objective of the present paper is to systematically replicate the emission from identical anatomic locations to document whether the anatomic percentage distribution pattern is generic. Part 1 includes the recording of ultra-weak photon emission from one sample subject over the torso, head and upper extremities with a highly sensitive charge-coupled device (CCD). Part 2 includes the analysis of that data to select a series of anatomic locations that were subsequently studied with a group of 20 subjects utilizing a highly sensitive, cooled and moveable (in three directions) photomultiplier system. Total sum emission of all recorded anatomic locations per subject fluctuates in this study almost 5-fold between subjects. However, the contribution of each anatomic location to the total emission from each subject was approximately the same percentage for each subject and similar to the sample CCD subject. The deviation of the anatomic percentage contribution for each subject was also established. The study presents evidence that there is a "common" anatomic percentage distribution pattern of ultra-weak photon emission for corresponding locations from each subject.

Keywords: Biophoton; Ultra-weak photon emission; Photon counting; Human body; Photon imaging; Spatial emission pattern

1. Introduction

Optical imaging of organisms has grown into an important tool in biomedical research. Novel macroscopic photonic imaging technologies in combination with emerging data analysis provide researchers with several techniques to visualize biological processes. A recent review focused on photographic and tomographic optical imaging techniques, bioluminescence and photoacoustic tomography [1]. The whole-body imaging technology exploring weak light, spontaneously emitted from humans without any artificially induced external excitation or stimulation, has been receiving relatively less attention, probably because the underlying biochemical and biophysical processes are not yet well established. The ultra-weak spontaneous emission is commonly referred to as "human biophoton emission". The intensity of this emission in the range 200–650 nm is estimated to be on the order of less than $\sim 10^2$ photons/cm^2 body surface [2]. Boveris et al. characterized photon emission from a variety of mammalian organs in an in vivo investigation of the radical reactions initiated by lipid peroxidation [3]. Many other pioneering studies have suggested the potential usefulness of non-invasive monitoring of oxidative metabolism and oxidative damage to tissue [4–6].

* Corresponding author. Tel.: +49 2182 825131; fax: +49 2182 825132.
E-mail address: meluna.wijk@wxs.nl (R. Van Wijk).

1011-1344/S - see front matter © 2005 Elsevier B.V. All rights reserved.
doi:10.1016/j.jphotobiol.2005.12.005

To study human photon emission and to clarify its basic mechanisms, one might use low-noise photomultiplier systems with high stability of the signal. Such a system exists suspended on runners in a light-tight dark room such that the detector head could be moved in three directions over a subject lying on a bed below [7]. A recent study utilizing this technology described a systematic multi-site recording of four subjects using 29 anatomic sites that were selected such that the distribution in photon emission could be studied as right–left symmetry, dorsal–ventral symmetry, and the ratio between the central part of the body and extremities [8,9]. Although data from that study demonstrated variability in patterns between subjects, some generic features were observed: (a) the thorax–abdomen region emits the lowest emission; (b) the hand and the head region emit the highest levels. The data also simultaneously suggested that a "common anatomic human biophoton percentage distribution emission pattern" exists corresponding to the above described levels of emission.

A second system to fundamentally characterize anatomic distribution of human ultra-weak photon emission utilizes two-dimensional imaging technology [10]. Recent developments demonstrate spontaneous ultra-weak biophoton emission from larger human anatomic sites using CCD imaging [11]. The few already published images also suggest a "common" anatomic human emission percentage distribution pattern.

This paper presents two sequential protocols used to register human biophoton emission patterns. The first protocol illustrates registration biophoton emission from the upper frontal torso, head, neck and upper extremities of a single subject utilizing CCD. Data obtained with the CCD illustrate the high or low emission from anatomic detection. The knowledge of such locations was subsequently utilized to select 12 anatomic spots for future recording of more subjects in a second protocol. The second protocol studied biophoton emission from those selected 12 anatomic spots from the frontal torso, head and hands of 20 healthy males. The data from this subsequent study illustrates the existence of a "common" human male body emission pattern amongst the simultaneous existence of individual differences. Fluctuations of emission intensity between subjects was not limited to a few body locations, but included the entire emission pattern.

2. Materials and methods

2.1. Subjects

Twenty subjects ranging in age from 20 to 65 years were, by self-report, healthy and free of medications and smoking. They were interviewed to exclude physical or emotional disorders. Written consent to participate in the study was obtained after they were thoroughly informed about the research. The emission of each subject was recorded only once.

2.2. Imaging human body with the highly sensitive charge-coupled device (CCD) camera

A cryogenically cooled CCD camera system that incorporates a CCD42-40 NIMO Back Illuminated High Performance CCD Sensor having full-frame architecture (CCD42-40, e2v technologies, UK) was used for imaging of human biophoton emission [12]. Operating temperature of the CCD sensor is −100 °C, resulting in a dark signal (electronic noise) of 0.65 e^-/pixel/h. Spectral response of the CCD ranges over 400–900 nm with quantum efficiency of >90% at the peak wavelength of 550 nm. The measurement was carried out in binning mode, resulting in the imaging format of 256 × 256 pixels. The magnification of the lens system for imaging torso and arms was approximately 0.03 and the magnification for imaging the face or hand was approximately 0.13. The CCD camera system was placed in a darkroom whose walls, ceiling, and floor were covered with non-fluorescent black cloth. The camera system was controlled from the laboratory located juxtaposition to the darkroom. The darkroom included a chair; the subject, after dark adaptation, was recorded in the sitting position. The duration of such measurement inside the darkroom was 30 min. Before measurement, subjects were already inside the darkroom for at least 30 min to prevent interference by delayed luminescence.

2.3. Recording human emission with the photomultiplier

The photomultiplier (9235 QB, selected type; Electron Tubes Limited, Ruislip, England; previously EMI) with a range of 200–650 nm was designed for manipulation in three directions [7,8]. It was mounted in a sealed housing under vacuum with a 52 mm diameter quartz window maintained at −25 °C to reduce the dark current. The dark current was measured before and after each experiment. During the experimental period the average background was 5.4 ± 0.3 cps (counts per second). A 7 cm long cone shaped extender is attached to the front of the photomultiplier tube allowing recording of emission from a 9 cm diameter anatomic area at a fixed distance. The front ring is vented inside, avoiding the condensation of moisture in the quartz window.

The photomultiplier was situated in a dark room juxtaposition to the control room housing the computer system. The walls and ceiling of the dark room were covered with mat black paint. The inner size of the dark room had the following dimensions: 2 m × 1.5 m × 2 m with an average temperature of 20 °C. The room could be vented. A bed was positioned in the dark room.

Subjects were commonly recorded between 11 a.m. and 2 p.m. Before recording, subjects were shielded from ambient light for at least 1 h to prevent interference by delayed luminescence [8,9]. Subjects remained during this period in the red dim light of the control room. Subjects then walked into the dark room and were positioned on the bed for at least 10 min. The photomultiplier tube was placed above

the body, the ring at the front port of the photomultiplier barely touching the body. The duration of each recording was 120 s consisting of 2400 time intervals of 50 ms.

2.4. Data analysis

Statistical analysis of photon count data was performed with Statistica 6.1 (StatSoft, Tulsa, OK, version 2004).

3. Results

3.1. CCD imaging and sequential multi-site recording with a photomultiplier of a single sample subject

The present technique of human CCD imaging, developed by one of the authors (Tohoku Institute of Technology, Sendai, Japan) is able to reveal the topography of spontaneous ultra-weak photon emission of dark-adapted human subjects. In this sequential study the cryogenic cooled CCD was utilized to image the ventral and dorsal sides of the torso and upper extremities of one sample dark-adapted subject (Fig. 1, panels A, D, G). The resulting set of large anatomic CCD images of this individual subject were obtained by recording continuously for 30 min at a distance of 100 cm. The images were compared with identically sized photographs of the subject taken under weak illumination (Fig. 1, panels B, E, H). As illustrated in the ventral image of the superior part of the body, photon emission intensity around the face and neck is highest and gradually decreases over the torso and subsequently over the abdomen. There also exists a gradual decrease in intensity from the superior central torso to its lateral dimensions. Dorsally, the highest intensity was emitted from the neck. The images of arm and hand of the subject illustrate that the low intensity of the body is extended over a large part of the arm and then increases over the hand.

The head and the hand are anatomically more complicated structures. For this reason CCD images of these anatomic locations were obtained at a distance of approximately 40 cm (Fig. 2). The image of the head demonstrates that the eyes exhibit a distinctly lower intensity (Fig. 2, panels A, B). Other locations such as forehead

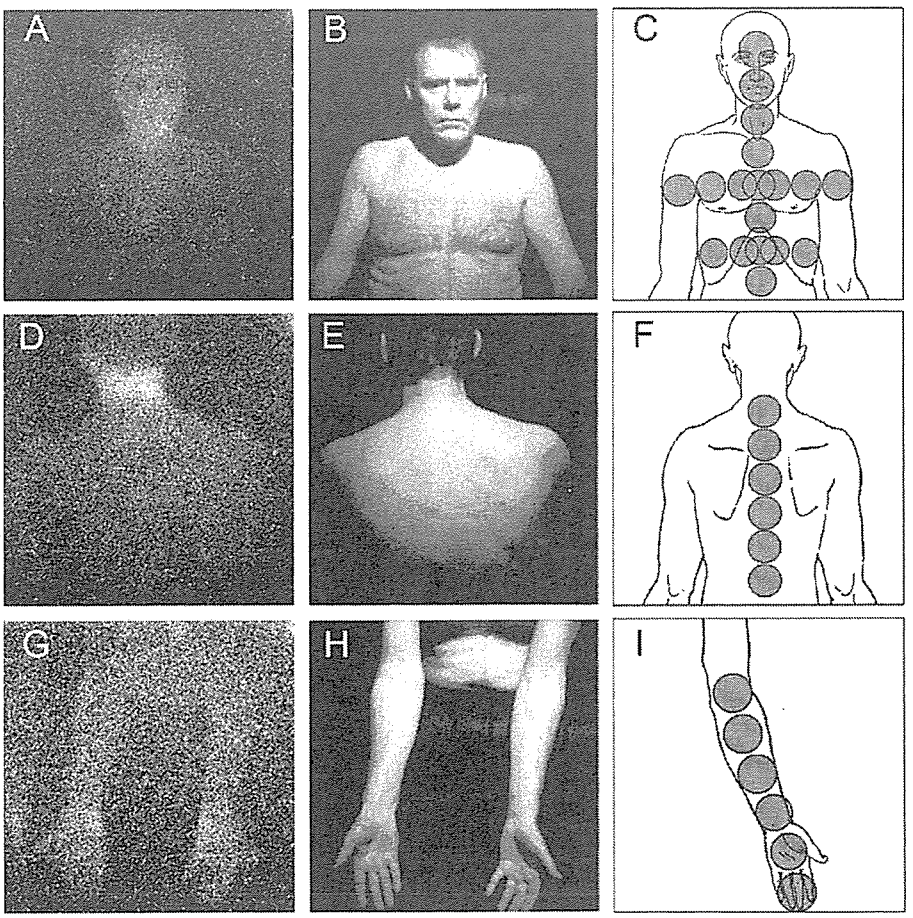

Fig. 1. Ultra-weak photon emission of the ventral and dorsal torso and arms of a human subject. Photon emission image measured with the CCD imaging system: ventral torso (A), dorsal torso (D) and arms (G). Corresponding photographs taken under weak illumination: ventral torso (B), dorsal torso (E) and arms (H). Anatomic locations used for recording of ultra-weak photon emission using the moveable photomultiplier: ventral torso (C), dorsal torso (F), arms and palms (I). Anatomic locations correspond with the respective emissions in Table 1.

and cheeks exhibit a rather homogeneous distribution of photon emission. The images of the palm and back of the hands illustrate more differentiation (Fig. 2, panels C, D). Emission between fingers fluctuates. Viewed from the palm (ventral) side, the four fingers demonstrate increased intensity from forefinger to little finger. However, the back (dorsal) side of the four fingers illustrates an increased intensity in the reverse order (little finger to forefinger). In addition, the dorsal side of the fingers and nails produce a high emission. A rather homogeneous photon emission distribution was present over the central palm and central back of the hand.

Subsequently, the locations illustrated in Fig. 1 (panels C, F, I) were used for quantitative measurements of photon emission utilizing the moveable photomultiplier device (International Institute of Biophysics, Neuss, Germany). Table 1 presents data along (a) the ventral and dorsal longitudinal axis from head to abdomen, (b) transversally from both left and right sides of the longitudinal axis, and (c) along arm and hand. The dorsal longitudinal axis illustrates lower intensities compared with the ventral. An exception is the high intensity around the neck.

The data collected transversely from both left and right anterior of the longitudinal axis were obtained from a 54 cm area over the breasts. Over the abdomen, data were reliably collected over a smaller (36 cm) transverse area. The central area has higher emission compared to the left and right sites.

Table 1
Spontaneous photon emission from body sites presented in Fig. 1

Photon emission (cps) from anatomic locations		
Location	Frontal	Dorsal
A. Longitudinal axis from head to abdomen (see Fig. 1C and F)		
Head	10.1 ± 0.3	
	13.5 ± 0.4	
Neck	14.8 ± 0.4	14.1 ± 0.3
Torso	12.5 ± 0.3	10.2 ± 0.3
	12.3 ± 0.4	8.5 ± 0.2
	11.5 ± 0.4	8.4 ± 0.3
	11.4 ± 0.4	9.0 ± 0.3
	10.8 ± 0.3	7.8 ± 0.3
Location	Breast	Abdomen
B. Transverse recordings (see Fig. 1C)		
Left-side	8.2 ± 0.4	
	9.7 ± 0.4	7.7 ± 0.3
Middle	11.9 ± 0.4	9.2 ± 0.4
	12.6 ± 0.4	9.5 ± 0.4
Right-side	9.7 ± 0.3	7.8 ± 0.3
	8.3 ± 0.3	
Location	Ventral	Dorsal
C. Locations from elbow to fingers (see Fig. 1I)		
Elbow	7.6 ± 0.3	7.1 ± 0.3
	7.5 ± 0.3	7.3 ± 0.3
	8.0 ± 0.3	7.7 ± 0.4
	9.7 ± 0.4	8.6 ± 0.4
	15.5 ± 0.4	12.1 ± 0.4
Fingers	15.6 ± 0.4	17.2 ± 0.5

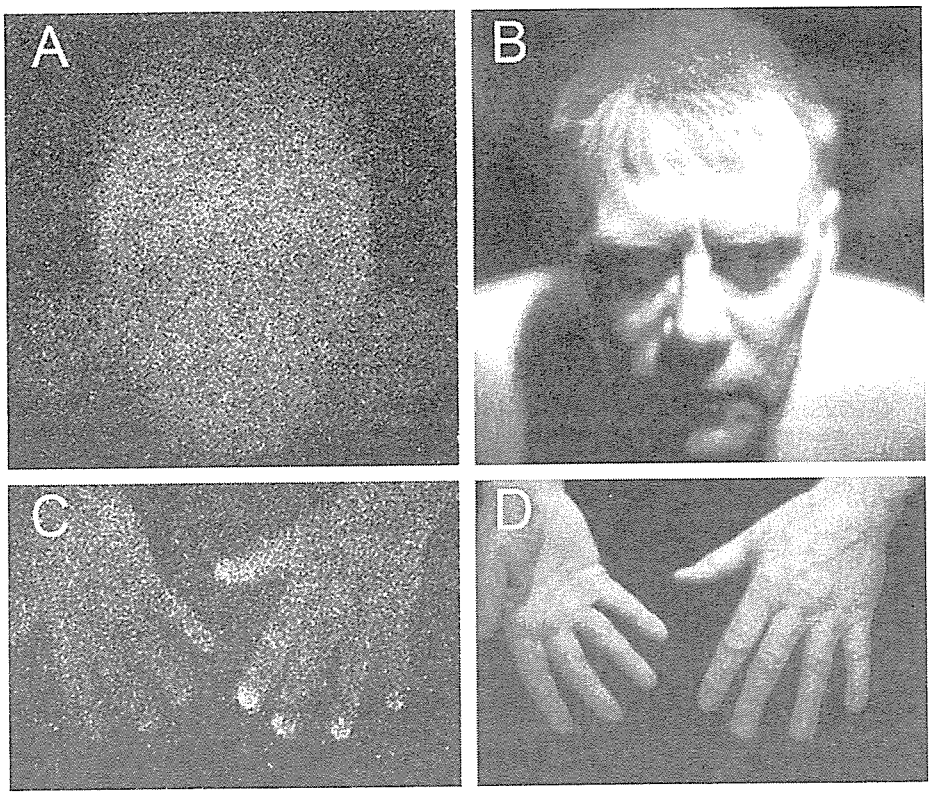

Fig. 2. Ultra-weak photon emission of the face, the palm and dorsum of the hand. Photon emission image measured with the CCD imaging system: face (panel A) and hands (panel C). The palm side is left and dorsum is right. Panels B and D are corresponding photographs under weak illumination.

The recording of photon emission along the arm and hand, both dorsally and ventrally, demonstrate that emission is low along the arm and strongly increases over the hands.

3.2. Multi-site registration of spontaneous emission from a group of male subjects utilizing the moveable photomultiplier

CCD data from the single subject described in Figs. 1 and 2 facilitated the selection of 12 full skin locations with uniform distribution of photon emission covering the wide range of intensities from low emission sites over the abdomen to high emission sites over the palms of the hand and forehead. The anatomic locations are presented in Fig. 3.

These locations were used to study whether anatomic distribution of emission reflects a "common" human anatomic percentage distribution emission pattern. It can be argued that (a) when one subject has a higher emission intensity than another subject at a specific anatomic location, it only reflects an increased emission at that location without any relationship to intensities at other locations, or (b) it reflects an increase of emission at all anatomic locations. In the latter case, each anatomic location should contribute in a proportional manner to the total emission. Therefore, the question whether there is a "common" human anatomic percentage distribution emission pattern can be answered when the emission contribution of each anatomic part of each subject to the total sum of emission is calculated for each subject.

The recordings at 12 anatomic locations were carried out with 20 control subjects. Each recording consisted of 2400 consecutive intervals of 50 ms. Recorded count values included electronic background which was subtracted in order to obtain the actual photon emission of the anatomic location. Electronic background did not change significantly during the day. However, background fluctuated during the experimental period (mid-October until mid-March) ranging between 4.9 ± 0.34 and 5.7 ± 0.42 cps (mean background 5.2 ± 0.41 cps). Thus, emission of each of the 12 anatomic locations of each subject was determined by subtracting the background value of the corresponding subject's recording session.

To estimate the contribution of each anatomic part of each subject to the total emission of that subject, total emission was defined as the sum value of the 12 recorded emissions. Fig. 4 portrays the contribution of each anatomic location to total emission for each subject.

Data demonstrate that the sum of emissions from 12 anatomic locations could differ by almost a factor of 5 between subjects; total emission can fluctuate between 51.22 and 231.97 cps. Each anatomic location's percentage emission from each subject statistically correlates ($p < 0.05$) with the total emission from each subject.

Extrapolation of each regression line approaches zero, suggesting that, in principle, each individual anatomic part participates in total emission with a constant percentage. The contribution of each anatomic location to total emission is not equal. The percentage of contribution is shown in Table 2. Photon emission from the abdomen was the lowest: values increased along the central axis rostally to the throat. Highest values were observed over the cheeks; emission again decreased at the forehead.

The data obtained with the photomultiplier correspond with the pattern of emission from the single CCD subject described in Fig. 1, reflecting a "common" human anatomic percentage distribution emission pattern.

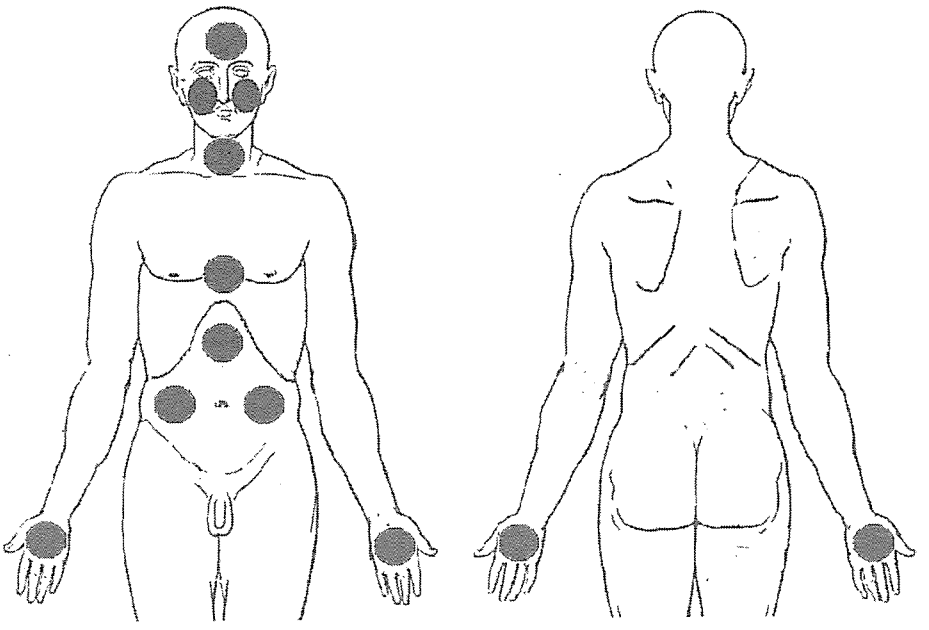

Fig. 3. Anatomic locations used to register spontaneous emission of 20 male subjects.

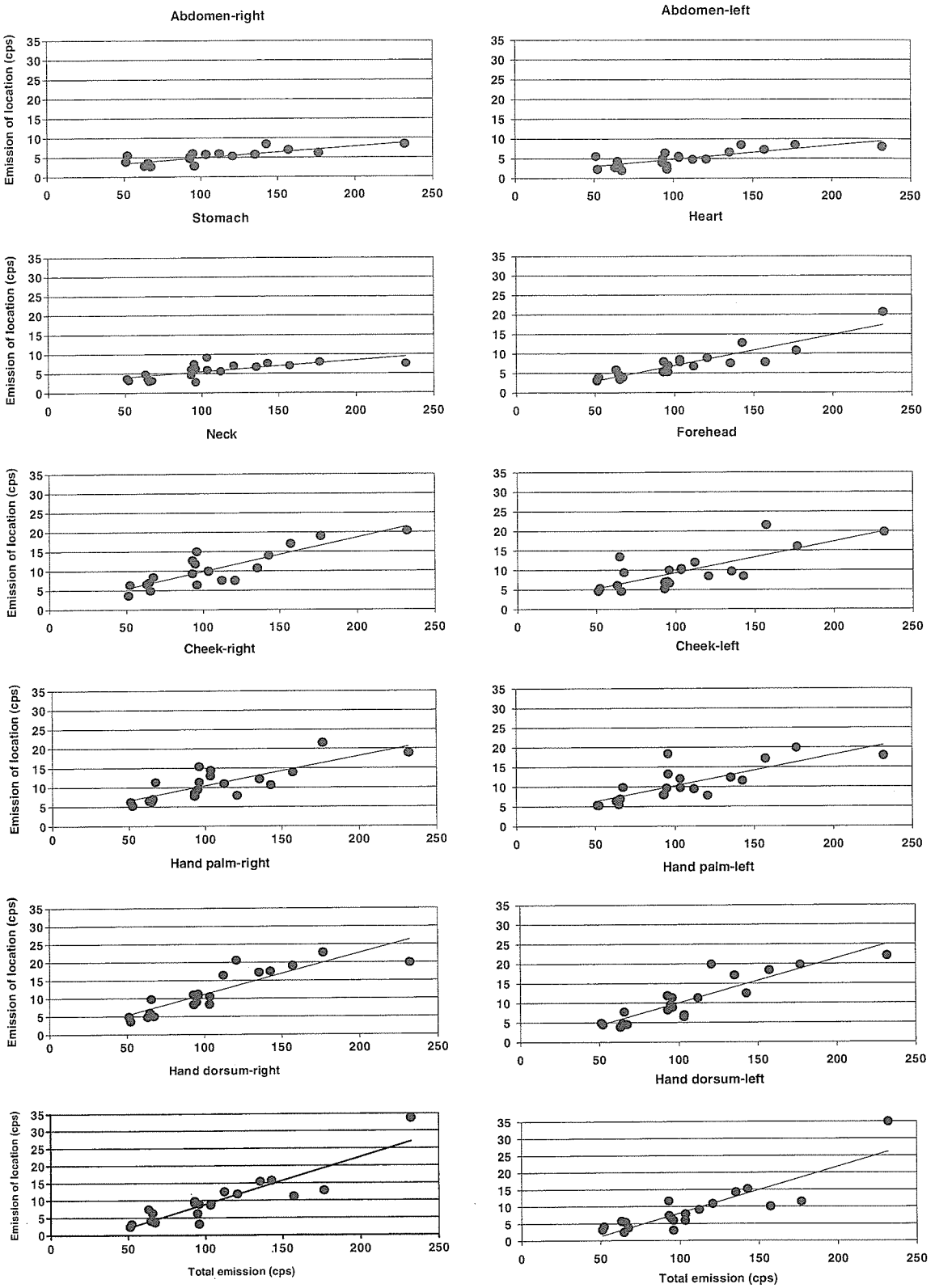

Fig. 4. Contribution of photon emission from individual anatomic locations to total emission for each subject. *X*-axis indicates total photon emission (counts/s); *Y*-axis indicates photon emission (counts/s) for each anatomic location. Each dot in a panel represents one subject, the presented line represents the best fit.

Table 2
Percentage contributions of photon emission from individual anatomic locations to total emission, and correlation of individual anatomic locations tot total emission

Anatomic location	Contribution (%)	Correlation coefficient
Abdomen-right	4.8	0.76 ($p < 0.05$)
Abdomen-left	4.7	0.78 ($p < 0.05$)
Stomach	5.3	0.70 ($p < 0.05$)
Heart	7.0	0.90 ($p < 0.05$)
Neck	9.8	0.85 ($p < 0.05$)
Cheek-right	10.3	0.80 ($p < 0.05$)
Cheek-left	10.1	0.78 ($p < 0.05$)
Forehead	9.2	0.77 ($p < 0.05$)
Hand palm-right	11.2	0.87 ($p < 0.05$)
Hand palm-left	10.1	0.89 ($p < 0.05$)
Hand dorsum-right	9.2	0.89 ($p < 0.05$)
Hand dorsum-left	8.4	0.87 ($p < 0.05$)

Data are derived from Fig. 4.

3.3. Deviations from the "common" human anatomic emission pattern

Even though data indicate that usually each anatomic location contributes in a proportional manner to the total emission, it also suggests that superimposed on the "common" human emission pattern, deviations are sometimes recorded for individual subjects. These deviations were analyzed to better understand how individual subjects as well as individual anatomic locations differ from the "common" pattern.

The analysis was completed in two steps: (a) the predicted photon emission was calculated for each subject and each anatomic location based on the total value and the percentage contributions from the different anatomic locations; (b) for each anatomic location and for each subject, the deviation from the mean for each subject was calculated (independent of its sign) and expressed as a percentage of the mean contribution of that anatomic location. The distribution of the deviations demonstrated that larger deviations seemed to occur with lower frequencies; only a few exceptionally large deviations were observed (Fig. 5).

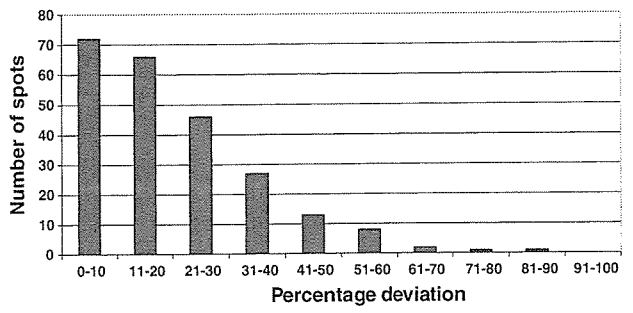

Fig. 5. Distribution of deviations from "common" pattern for all measured spots (n =240). Percentage deviation was calculated according to the text.

Table 3
Average deviations of different anatomic locations from "common" anatomic percentage distribution pattern of photon emission

Anatomic location	Average deviations (%) from "common" pattern
Abdomen-right	25.3 ± 5.9
Abdomen-left	23.8 ± 6.5
Stomach	21.5 ± 4.1
Heart	16.9 ± 2.0
Neck	19.9 ± 3.5
Cheek-right	19.6 ± 3.8
Cheek-left	18.7 ± 4.6
Forehead	25.3 ± 6.2
Hand palm-right	20.3 ± 3.0
Hand palm-left	20.4 ± 3.5
Hand dorsum-right	24.7 ± 4.0
Hand dorsum-left	26.4 ± 4.7

The average deviation for each specific anatomic location is presented in Table 3. Data demonstrated deviations between 16.5% and 25.4%. The area around the heart exhibited the lowest fluctuations indicating that the contribution of emissions of that anatomic location to total emission is similar for all subjects. Deviations differ more over the abdomen, head and hand.

The average deviation for individual subjects is presented in Table 4. Data indicated that these average deviations range between 12.5% and 40.5%. Eighty-five percent of the subjects demonstrated an average deviation not exceeding 30% of the values expected on the basis of a "common" pattern.

4. Discussion

This study provides evidence that humans have a "common" pattern of ultra-weak photon emission from the

Table 4
Average deviation of different subjects from "common" anatomic percentage distribution pattern of photon emission

Subject	Average subject's deviation (%) from "common" pattern
1	20.7 ± 4.6
2	16.1 ± 2.2
3	17.6 ± 4.6
4	17.0 ± 2.6
5	28.2 ± 10.0
6	23.8 ± 9.5
7	24.9 ± 5.7
8	21.4 ± 3.4
9	14.0 ± 3.2
10	12.7 ± 3.1
11	22.1 ± 5.0
12	19.3 ± 3.2
13	14.0 ± 2.9
14	17.7 ± 4.1
15	32.0 ± 10.3
16	34.4 ± 4.3
17	28.9 ± 6.1
18	17.3 ± 3.6
19	13.9 ± 2.2
20	42.0 ± 7.9

superior anatomic parts of the body including the upper extremities. The abdomen emits the lowest intensity, which gradually increases rostally and is the highest around the face. High emission values were also documented for the hand. The pattern corresponds with photon emission images utilizing the highly sensitive technology of the CCD42 family of CCD sensors. This sensor, in combination with back thinning and extremely low noise amplifiers, allows the imaging of large area human photon emission with high resolution. The contrast of the large body images is determined by the spatial shot noise of the dark current. Signal noise ratio can be increased by expansion of the exposure time or reduction of the spatial resolution. The present images were obtained according to the technical specifications in the section on methods without further reduction of the spatial resolution.

Neither the "pattern" of emission nor the differences between subjects reflect delayed luminescence after exposure to light prior to recording. Such is excluded by sufficient adaptation to dark room conditions prior to measurements [8,9]. The emission pattern is also not explained by reflection of light from "high-emission" anatomical regions of the body, because emission intensity is too low.

The emission pattern in CCD images was recorded, utilizing a spectral sensitivity in the 400–900 nm range. The spectral sensitivity of the moveable photomultiplier was limited to the range of 200–650 nm. Research with the moveable photomultiplier has demonstrated that human photon emission was at wavelength more than 430 nm, independent of the body location [8,9]. Future studies need to quantify the specific contribution of the different parts of the spectrum to emission of different anatomical locations of different subjects.

The etiology of the "common" pattern of emission is presently unknown. The abdomen housing predominantly soft tissues presents the lowest emission, whereas the head and hands containing highly structured bone exhibit the highest emission. Further research is required to clarify relationships between emission and anatomic areas. Might this suggest a lack of electrical field homogeneity over the body surface?

Subjects demonstrated a pattern of emission that closely resembles a "common" pattern with only minor deviations over specific anatomic locations. In contrast, a few subjects exhibited larger deviations. The average deviation of individual subjects from the "common" pattern ranged between 12.5% and 40.5%. The dynamic character of the deviations is currently under investigation. The initial pilot data acquired with four subjects demonstrated that emission values of individual subjects could fluctuate during the daytime. Photon counts over the body were lower in the morning than in the afternoon with the thorax–abdomen region emitting the least and most constant emission. However, the upper extremities and the head region emitted the highest levels which increased during the daytime. It was evident that total emissions varied, whereas the "common" pattern remained almost similar during the day. Further research is required to detect if specific anatomic regions are physiologically regulated in different ways. Such research might lead to new insights regarding differential physiologic/metabolic processes involved in ultra-weak photon emission.

5. Abbreviations

CCD charge-coupled device
cps counts per seconds

Acknowledgements

This work was supported by the Samueli Institute of Information Biology and the Rockefeller-Samueli Center for Research in Mind-Body Energy. The authors thank Dr. Fritz-Albert Popp and Dr. Yu Yan for their support. The authors also thank Dr. John Ackerman for his assistance in editing the text.

References

[1] V. Ntziachristos, J. Ripoll, L.V. Wang, R. Weissleder, Looking and listening to light: the evolution of whole body photonic imaging, Nature Biotechnol. 23 (2005) 313–320.
[2] R. Van Wijk, E.P.A. Van Wijk, An introduction to human biophoton emission, Forsch. Komplementärmed. Klass. Naturheilkd. 12 (2005) 77–83.
[3] A. Boveris, E. Cadenas, R. Reiter, M. Filipkowski, Y. Nakase, B. Chance, Organ chemiluminescsence: noninvasive assay for oxidative radical reactions, Proc. Natl. Acad. Sci. USA 77 (1980) 347–351.
[4] E. Cadenas, A. Boveris, B. Chance, Low-level chemiluminescence of biological systems, in: W.A. Proyer (Ed.), Free Radicals in Biology, vol. VI, Academic Press, New York, 1984, pp. 211–242.
[5] G. Sauermann, W.P. Mei, U. Hoppe, F. Stäb, Ultraweak photon emission of human skin in vivo: influence of topically applied antioxidants on human skin, Meth. Enzymol. 300 (1999) 419–428.
[6] H. Sies (Ed.), Oxidative Stress: Oxidants and Antioxidants, Academic Press, New York, 1991.
[7] S. Cohen, F.A. Popp, Biophoton emission of the human body, J. Photochem. Photobiol. B 40 (1997) 187–189.
[8] E.P.A. Van Wijk, R. Van Wijk, Multi-site recording and spectral analysis of spontaneous photon emission of human body, Forsch. Komplementärmed. Klass. Naturheilkd. 12 (2005) 96–106.
[9] R. Van Wijk, E.P.A. Van Wijk, Human biophoton emission, Recent Res. Develop. Photochem. Photobiol. 7 (2004) 139–173.
[10] M. Usa, H. Inaba, Spontaneous photon emission from human body, Med. Imag. Technol. 13 (1995) 47–54.
[11] M. Kobayashi, Modern technology on physical analysis of biophoton emission and its potential extracting the physiological information, in: F. Musumeci, L.S. Brizhik, M.W. Ho (Eds.), Energy and Information Transfer in Biological Systems, World Scientific Publishing, New Jersey, London, 2003, pp. 157–187.
[12] Technological Report A1A-CCD42-40 NIMO Back illuminated Issue 4, April 2003. Available from: <http://e2vtechnologies.com/datasheets/charge_coupled_devices_ccds/ccd42-40_nimo_bi.pdf>.

cancer with low/no expression in normal tissues. Immunohistochemical studies with antibodies against DD-O11O revealed strong tumor cell surface staining in a majority of human ductal and lobular breast adenocarcinomas, breast cancer metastases and serous ovarian epithelial cancers. We further showed that DD-O110 protein is extensively glycosylated and displayed on the surface of cultured breast tumor cell lines. Other groups recently identified a new member of the B7 immunomodulatory protein family, B7-H4, which is identical to DD-O110. B7-H4 protein is expressed on the surface of a variety of activated immune cells and functions as a negative regulator of T cell responses. Thus overexpression of B7-H4 by human cancers may inhibit an anti-tumor immune response. We have obtained additional data for a functional role of B7-H4 in cancer showing that this protein can promote tumor formation when overexpressed in tumor epithelial cells. We generated monoclonal antibodies which recognize native human DD-O110 protein and bind efficiently to the surface of live human tumor cell lines as well as to human breast or ovarian cancer samples. Antibodies bound to B7-H4 on tumor cells can effectively internalize. The restricted normal tissue distribution of B7-H4, its over-expression in a majority of breast and ovarian cancers together with a functional role in promoting tumor growth make this cell surface protein an ideal target for a monoclonal antibody therapeutic strategy. Efficacy studies with a set of promising monoclonal antibodies are in progress.

SP29
AN ASSESSMENT OF THE INTERACTION OF MITOMYCIN C AND DOXORUBICIN IN EMT6 MOUSE MAMMARY TUMOR CELLS

Shuhendler A., O'Brien P., Rauth A. and Wu X.
University of Toronto, Toronto, ON, Canada

The co-application of the chemotherapeutic agents mitomycin C and doxorubicin has been shown to result in supra-additive tumor cell killing *in vitro* and *in vivo*. Here, we determined if this interaction was truly synergistic and defined the parameters that enabled the intracellular interaction of these drugs. The median effect analysis (MEA) was used to determine the degree of interaction, as it is free from bias and mechanistic assumptions. To determine the parameters important for this interaction, formaldehyde and reactive oxygen species formed from drug metabolism were measured, and DNA cross-linking and DNA double-strand breaks were followed as genotoxic endpoints. In addition glutathione levels were modulated, and major metabolizing enzymes (i.e. DT-Diaphorase and CYP450) were inhibited in whole cells. The interaction of mitomycin C and doxorubicin was found to be a true synergy. *In vitro* evidence identified glutathione levels in the cell as an important mediator of this interaction, and thus mitomycin C-derived products of metabolism (e.g. formaldehyde, mitomycin C reactive metabolites) that are known to deplete glutathione as potential players. Since DNA cross-links were found to only increase additively with co-administration of the drugs, we propose that the poisoning of topoisomerase II-alpha by doxorubicin interacts with the drug-induced DNA cross-links. Therefore, the synergy observed between mitomycin C and doxorubicin may be elicited through mitomycin C-derived formaldehyde and reactive metabolites, glutathione depletion and the enhanced genotoxicity of the combination of DNA cross-links and topoisomerase II-alpha poisoning.

SP30
NANOSIZED SILVER IODIDE BEADS AS NEW CONTRAST MEDIA FOR SENTINEL LYMPH NODE NAVIGATION SURGERY

Sakurai Y.[1], Takeda M.[1], Kawazoe Y.[2], Kasuya A.[2], Kobayashi Y.[3], Kamei T.[1], Nakajima M.[1] and Ohuchi N.[1]
[1]Graduate School of Medicine, Tohoku University, Sendai, Japan; [2]Institute for Materials Research, Tohoku University, Sendai, Japan; [3]School of Engineering, Ibaraki University, Hitachi, Japan

The objective of this study was to evaluate the possibility of the new nanosized silver iodide beads (AgI) with silica coating as a X-ray contrast medium. Silica coating was performed to prevent acute and fatal reactions. We tried to apply AgI for Sentinel Lymph Node Biopsy (SNB). Some institution reported the effectiveness of X-ray CT method for identifying sentinel lymph node (LN). But traditional contrast media go through LN so quickly that it is diffucult to detect LN precisely.As the size of beads determines staying and passing time in the LN, we can control enhancement period by modifying the size of beads. We also assessed its temporal distribution with X-CT after subcutaneous and intravenous AgI injection to a rabbit. The contrast-enhancement of a blood vessels, lymph

nodes, the liver and the spleen was observed. Compared with existing contrast media, AgI showed delayed washing out. We can carry out SNB with AgI beads in most institutions which have X-ray equipment and can detect sentinel lymph node more precisely than radio isotopes before surgical treatments. In addition, AgI nanoparticles can prevent allergic reactions by silica coating. AgI are expected to be employed in clinical fields by further examination in the future.

SP31
IN VIVO ROLE OF THE SIX1 HOMEOPROTEIN IN MAMMARY GLAND TUMORIGENESIS

McCoy E.[1], Abbey N.[1], Coletta R.[1], Jedlicka P.[1], Chodosh L.[2] and Ford H.[1]
[1]*University of Colorado Health Sciences Center, Aurora, CO, USA;* [2]*University of Pennsylvania, Philadelphia, PA, USA*

Human Six1 is a homeodomain-containing transcription factor that is critical for the expansion of precursor populations during development. In addition to its developmental role, overexpression of Six1 has been detected in a number of human cancers, including breast cancer, where it is linked to both proliferation and metastasis. As many as 50% of primary breast cancers and 90% of metastatic lesions overexpress the gene, in part due to gene amplification. Six1 can transform a mammary epithelial cell line, but no work has been done to show the effects of Six1 overexpression *in vivo*. We have established an inducible, mammary-specific Six1 overexpression model by crossing MMTV-rtTA mice to TetO-Six1 mice, and are using this model to test whether Six1 overexpression leads to mammary tumors, as well as to dissect the molecular mechanism by which Six1 influences tumorigenesis *in vivo*. Data from this model are suggestive of both a developmental and tumorigenic phenotype. Overexpression of Six1 throughout pregnancy and lactation leads to an increased frequency of litter loss and decreased pup weight, suggesting that Six1 overexpression impairs lactation and normal mammary differentiation. In mice induced to overexpress Six1 in the mammary gland for 5 months, a hyperprolifative phenotype is observed. Furthermore, preliminary data indicate that invasive mammary adenocarcinoma is observed with long latency and constitutive Six1 overexpression. Data from this model suggests that inappropriate expression of Six1 impairs differentiation and promotes tumorigenesis. This inducible model provides us with a system to examine whether removal of Six1 expression can reverse the phenotypes, thereby addressing whether Six1 is a viable drug target. Importantly, Six1 is not necessary for most normal adult tissues, and thus therapies directed against Six1 may not lead to the severe side effects seen with more conventional treatments.

SP32
IDENTIFICATION OF TARGET GENES MEDIATING GROWTH INHIBITION BY THE TRANSCRIPTION FACTOR C/EBP DELTA

Pawar S., Sharan S. and Sterneck E.
National Cancer Institute, Frederick, MD, USA

The transcription factor C/EBPdelta promotes apoptosis of mammary epithelial cells during mammary gland involution. Furthermore, overexpressed C/EBPdelta inhibits the growth of certain human breast tumor, prostate tumor and leukemia cell lines. In the mouse mammary gland, C/EBPdelta promotes mammary epithelial cell apoptosis during post-lactational involution. The direct downstream targets of C/EBPdelta mediating growth arrest and/or apoptosis in breast epithelial cells however are unknown.
Cyclin D1 is an important regulator of the cell cycle and frequently overexpressed in breast tumors cells. Emerging evidence suggests that cyclin D1 might also act through pathways other than as a cell cycle regulator. Given its importance in tumorigenesis, understanding the transcriptional regulation of the cyclin D1 promoter may help in the identification of molecular targets.
Our data suggest that cyclin D1 expression is regulated by C/EBPdelta in breast epithelial cells. Overexpression of C/EBPdelta in mammary epithelial cells resulted in down regulation of cyclin D1 levels. By chromatin immunoprecipitation assay, EMSA and reporter assays, we identified at least one element in the cyclin D1 promoter that is targeted by C/EBPdelta. Thus, our data suggest that C/EBPdelta promotes growth arrest and apoptosis in part via the down regulation of cyclin D1 promoter.

3956 breast and/or ovarian, prostate, colorectal and male breast cancer cases and 3591 controls.
Results: The frequency of Cys557Ser appeared to be increased among familial breast and/or ovarian cancer cases when compared to healthy controls (p=0.001).
Conclusion: Our results provide further evidence that *BARD1* Cys557Ser confers a slightly increased risk of breast cancer.

SP10
DETECTION OF SENTINEL LYMPH NODES BY NOVEL MR CONTRAST MEDIA

Takeda M.[1], Kobayashi Y.[2], Sakurai Y.[3], Cong L.[3], Ishida T.[3], Suzuki A.[3], Amari M.[3] and Ohuchi N.[3]
[1]Graduate School of Engineering, Tohoku University, Sendai, Japan; [2]Ibaraki University, Hitachi, Japan; [3]Graduate School of Medicine, Tohoku University, Sendai, Japan

Sentinel lymph node (SN) navigation surgery has been widely accepted as a method for made-to-order and low-invasive medicine. The size of particles is the most important factor for SN detection. We previously decided the suitable size for SN detection as 40nm by animal experiments. In this study, we aimed to clarify possibility of nano-sized particles of MR contrast media with appropriate size to make up disadvantages of existing methods like radioisotope or dye methods.
We developed nano-sized gadolinium beads in size of 40-60nm. We took MR imaging of the suspension of gadolinium nano-particles. And we injected the suspension of gadolinium beads into the rat's foot pad of the hind leg subcutaneously and followed MR scanning of the inguinal area for SN detection.
The nano-sized gadolinium beads exhibited higher signal intensity than water. It also showed changes of signal intensity in inguinal lymph nodes.
Existing contrast media for MRI passes so fast through lymph nodes that the timing of administration is difficult. As appropriate sizes allow nano-particles to stay at lymph nodes for a while, we could detect gadolinium nano-particles before and during surgery like radioisotopes. In conclusion, we claim that the nano-sized gadolinium beads have a potential to be an alternative to existing tracers for SN detection.

SP11
APPLICATION OF NANOTECHNOLOGY FOR BREAST CANCER RESEARCH: NANO-DDS AND MOLECULAR IMAGING BASED ON VISUALIZATION OF SINGLE PARTICLE IN VIVO

Ohuchi N.[1], Takeda M.[2], Nakajima M.[1], Sakurai Y.[1], Kawai M.[1], Ishida T.[1] and Higuchi H.[3]
[1]Graduate School of Medicine, Tohoku University, Sendai, Japan; [2]Graduate School of Engineering, Tohoku University, Sendai, Japan; [3]Biomedical Engineering Research Organization, Tohoku University, Sendai, Japan

Nanomedicine is the application of nanotechnology to prevention, diagnosis and treatment of human disease. It has a potential to change medical science dramatically in the 21st century. However, the research field is in its infancy, and it is necessary to grasp mechanism of pharmacokinetics, the toxicity on the occasion of application to medical treatment, in particular on the aspect of safety of the materials and devices. Here, we describe fluorescent nono-particles for sentinel node navigation for breast cancer surgery in experimental model, which have shown the potential to be an alternative to existing tracers in the detection of the sentinel node of if we select the appropriate particle size and wavelength. We also describe generation of CdSe nanoparticles, Quantum Dots (QDs) conjugated with monoclonal anti-HER2 antibody, Trastuzumab, for molecular imaging of breast cancer cells. The QDs-Trastuzumab complex coated with PEG was successfully made without decreasing the titer of antibody. We established a high resolution of 3D in vivo microscopic system as a novel imaging method at molecular level. The cancer cells expressing HER2 protein were visualized by the nanoparticles in vivo at subcellular resolution, suggesting future utilization of the system in medical applications including drug delivery system to target the primary and metastatic tumors. Future innovation in cancer imaging, not only at cellular level but also at molecular level, by synthesizing diagnostic agents with nanoparticles, is now expected.